

Microstructural and Mechanical Characterization of Variability in Porous Advanced Ceramics using X-ray Computed Tomography and Digital Image Correlation

Calvin Lo^{a,*}, Tomoko Sano^b, James D. Hogan^a

^a*Department of Mechanical Engineering, University of Alberta, Edmonton, AB T6G 2R3, Canada*

^b*Weapons and Materials Research Directorate, Army Research Laboratory, Aberdeen Proving Ground, MD 21005, USA*

Abstract

This paper explores microstructural and mechanical variability in porous ceramics, combining advanced X-ray computed tomography (XCT) and digital image correlation (DIC) techniques to characterize an alumina material. The results show low variability in microstructure, with median pore size values for this alumina ranging from 16.0 μm to 17.2 μm across ten samples. Spatial analysis showed internal pores are regularly distributed, and though spacing was found to be largely independent of pore size, the variability in spacing was shown to be greater for smaller pores. Mechanical results show a strain-rate dependence and greater scatter at quasi-static rates, with the coefficient of variation for compressive strength and failure strain decreasing from 10.28% and 10.23% at quasi-static to 5.20% and 4.17% at dynamic rates. In view of the consistency demonstrated in the microstructure, the difference in variability between the quasi-static and dynamic mechanical properties is attributed to variability in testing conditions (e.g. misalignment of platens) and the activation of a greater number of pores in dynamic compression. In summary, these results motivate the use of new spatial characterization parameters via XCT for links to manufacturing, the integration of realistic microstructures into computational models,

*Corresponding author
Email address: c1o2@ualberta.ca (Calvin Lo)

and focus on the role of defect distributions in dynamic compressive failure events.

Keywords: X-ray computed tomography, microstructure, digital image correlation, defect, variability

1. Introduction

Advanced ceramics commonly serve as critical structural components in body armor[1], tooling[2], and prosthetic[3] applications. To optimize the processing of advanced ceramics for these applications, it is important to consider the role of microstructural defects in the brittle failure process. Microstructural defects such as pores or secondary phase inclusions can arise due to incomplete densification or the use of excess sintering aids[4]. Under compressive loading, like in impact, these pre-existing defects serve as stress concentration sites[5], degrade bulk material properties[6], and have a significant influence on fragmentation behaviour[7]. Physics-based models have been developed to account for the effects of internal defects on the mechanical properties[8, 9] and dynamic failure[10, 11, 12] of brittle materials.

To accurately capture the effects of pre-existing flaws, defect characteristics are required as model inputs. However, while average defect size, volume fraction, and number density are common model inputs, parameters relating to defect orientation and spatial distribution have received limited consideration in theoretical and characterization studies. Furthermore, most single value characterization parameters are limited in that they do not account for the variability in defect characteristics. Owing to a lack of 3D characterization data in advanced ceramics, 3D models often rely on the use of data from 2D characterization studies, and microstructural inputs in computational models are frequently idealized in the absence of characterization data.

X-ray computed tomography (XCT) is well-suited for the 3D characterization of inhomogeneous microstructures in advanced ceramics. XCT is a visualization technique that relies on the contrasts in x-ray attenuation within a material to image internal features. Past defect characterization studies typically utilized optical or scanning electron microscopy to image microstructural features [13, 14]. However, microstructural flaws are distributed throughout the volume of the material, and traditional imaging techniques require either very thin samples or serial sectioning of the sample to observe internal flaws [15]. In

addition, 2D characterization tools are limited in their ability to fully capture the size or geometry of 3D features. In contrast, XCT can visualize internal features non-destructively and access 3D geometries. With the availability of current computed tomography systems, it is possible to resolve microstructural features on the scale of microns across scan volumes on the scale of cubic millimeters. As a result, there has been an increased focus on the use of XCT for the quantitative characterization of microstructures in a variety of materials in recent years (e.g., boron carbide [16], composites [17], and titanium alloys [18]).

With this in mind, this paper is motivated by the works of Li et al.[19, 20], whose efforts focused on methods for 3D characterization of inhomogeneous microstructure, and Graham-Brady[21], whose modeling work highlighted the effects of defect spatial distributions on the variability of the strength of materials. Building on the works of the motivating papers, this paper will explore the pore characteristics and mechanical behaviour of aluminum oxide (Al_2O_3), an advanced ceramic that has commonly been used in armor components. XCT was applied to characterize the pores, with a focus on improving methods for interpreting 3D data that can be generalized to future ceramic systems. Characterization parameters relating to pore size, morphology, orientation, and spatial distribution were evaluated to assess microstructural variability across multiple samples. Following pore characterization, compression experiments were performed at quasi-static and dynamic strain rates to determine the link between mechanical and microstructural variability. This paper will conclude by discussing the results in the context of manufacturing, computational model parameters, and rate-dependent failure mechanisms in brittle materials. The improved characterization techniques and mechanical results presented will advance the development of advanced ceramics.

2. Experimental Method

2.1. Material

XCT characterization and compression experiments were performed on AD85 alumina from CoorsTek Inc.(Vista, California, US)[22]. Table 1 shows manufacturer values for AD85 material properties. Previous microstructural characterization performed by the authors on AD85 have shown that the dominant form of meso-scale defect in AD85 microstructure are isolated intergranular pores[23].

This material was selected because the pore sizes observed in AD85 are compatible with the resolution of the XCT scanner used for this study, and alumina is a common armor material. Figure 1(A) shows a schematic of the specimen, specifying the geometry and load direction. Ten cuboidal specimens measuring 2.3 mm by 2.7 mm by 3.5 mm in size were machined from different locations on multiple CoorsTek Inc. AD85 tiles. The small size of the specimen was chosen to accommodate the strength of the Kolsky bar used for dynamic compression, as well as the synchrotron x-ray source used for high resolution imaging. The cuboidal shape was chosen so that a flat sample surface could be visualized during compression experiments (as shown in Figure 1(B)) for 2D digital image correlation measurements, as will be discussed later in the Mechanical Testing section. The samples were cut from the tile with the long dimension of the sample parallel to the shortest dimension, or thickness, of the tile.

2.2. X-ray Computed Tomography Analysis

2.2.1. X-ray Computed Tomography Scans

Microstructural characterization was performed using X-ray computed tomography. All following microstructural analysis is performed using the digital reconstruction of defects visualized through XCT. XCT scans of the samples were carried out at the Biomedical Imaging and Therapy (BMIT) beamline at the Canadian Light Source synchrotron facility (Saskatoon, Saskatchewan, Canada). Synchrotron radiation is ideal for high resolution computed tomography due to its high intensity, which produces a high signal to noise ratio. The

scans were carried out at the 05B1-1 POE-2 endstation[24] using a monochromatic beam. All images were captured using the ORCA-Flash 4.0 camera in conjunction with the Hamamatsu AA60 detector. For each specimen, 3001
90 projections were taken over 180° of rotation, and 799 tomograms were reconstructed. Each scan has a voxel size of $3\ \mu\text{m}$. Figure 2(A) shows a reconstructed cross-section of the AD85 microstructure in a representative scan (AD85 01). A low-pass Gaussian filter was applied to the sinograms to remove ring artifacts. Dark speckles in the scan represent pores while the gray area represents the
95 alumina grains. Individual grains cannot be resolved at this scale. The scan volume was large enough to encompass the entire sample, however, edge effects distort features near the corners and edges of the specimen. To avoid the distorted regions, only the central volume consisting of a cylinder with a height of 2.1 mm and a diameter of 2.7 mm was considered for analysis of pore size,
100 shape, and spatial distributions.

2.2.2. Image Segmentation and Filtering

All image segmentation and data analysis was performed on MATLAB (2018a, Natick, US). The first step of the analysis was to apply image segmentation to identify the pores in the XCT scans. The segmentation process divides pixels
105 in the scans into foreground (1's) and background (0's) pixels, generating binary images where foreground pixels represent pore area. Due to a difference in X-ray attenuation, the void in a pore will show up with a different range of grayscale values from the adjacent alumina grains. This contrast in grayscale values can be used to isolate pores, or any other discernible features,
110 by grayscale thresholding. The choice of the grayscale threshold will affect the accuracy of the segmentation, and over-segmentation of pores in this step of the process can introduce noise into characterization results later. To minimize noise from possible over-segmentation, segmentation was performed using adaptive local thresholds. Unlike global thresholds, which are typically chosen
115 based on the intensities of pixels in the entire image, locally adaptive thresholds are computed based on the mean intensity of pixels in the neighborhood of

each pixel. Rather than dividing all pixels into foreground and background by a single global threshold, this method uses a local threshold for each pixel to make the determination between foreground and background. Segmentation by
120 locally adaptive thresholds is more robust to scan artifacts and contrast changes than global thresholds because it takes into account local grayscale contrasts[25]. There is insufficient contrast in the XCT scans in this study to differentiate between the glassy phase from the alumina grains, so there is no risk of locally thresholding microstructural constituents other than pores. Figure 2(B) shows
125 the binary segmented cross-sections, where the black background represents alumina grains and the white dots, the foreground, represents pores. The binary images resulting from segmentation were then combined into a 3D matrix, and connected components analysis (using 26 connectivity) was performed to identify individual three-dimensional pores. Figure 2(C) shows a rendering of
130 a set of 3D reconstructed pores, which is the culmination of the segmentation process and connected components analysis. The microstructural analysis in the following sections are carried out using these sets of digitally reconstructed pores.

Sampling limitations related to the voxel must be considered when perform-
135 ing analysis on XCT reconstructions. The voxel is the three-dimensional analog of the pixel, and it defines the smallest volume that can be represented digitally. However, this is not the same as the smallest *resolvable* volume. For every three-dimensional object reconstructed from XCT scans, pixels from multiple cross-sections must be combined to reconstruct the volume. Consequently,
140 a lower limit on the number of voxels required to adequately represent a single object should be set to exclude from the analysis features that cannot be properly resolved. In addition, applying a minimum volume limit will eliminate noise generated from over-segmentation, which are typically small in size and randomly located in space. For these reasons, the total set of reconstructed
145 pores for each specimen in this study were filtered by a minimum of 8 voxels, a resolution limit consistent with those used in the literature [18, 26, 27].

2.2.3. Ellipsoid Representation of Pores

In past optical microscopy and SEM characterization studies [13, 15], the pore size was typically defined as the equivalent diameter, which is the diameter of a circle with the same area as the observed pore. This idea can be extended to three dimensions and the equivalent diameter can be defined as the diameter of a sphere with the same volume as the reconstructed defect. However, this definition does not adequately characterize the length of non-spherical pores, where the span of the pore will differ depending on the direction. Furthermore, the characteristic length of interest in micro-mechanical models is often the longest length spanned by a general defect[28], which may be underestimated by this method. Defect morphology is also often characterized by sphericity, which compares the ratio of the defect circumference to area, or surface area to volume in three-dimensions. Both characterization definitions essentially model defects as circles, or spheres in three-dimensions, but defects in ceramics can take on a variety of shapes. For instance, graphitic inclusions in boron carbide have been found to be disk-like in three-dimensions[7], and Carniglia[8] has commented that intergranular pores in polycrystalline ceramics typically have moderate to high aspect ratios. For these types of defects, a spherical definition will not accurately capture the defect size or shape. This is an important consideration as theoretical works have shown that the pore shape has a significant effect on the macroscopic compliance[29, 30], and past investigators have emphasized the importance of incorporating pore geometry when modeling the effects of porosity on mechanical properties[8, 31].

Based on qualitative assessments of the XCT scans and digital reconstructions in this study, the majority of pores in AD85 alumina are closed, non-overlapping, and have a convex shape. The reconstructed pores are therefore well-suited to ellipsoidal representation. To fit an ellipsoid to the reconstructed pore, we compute the co-variance matrix of the (x,y,z) coordinates of the voxels that make up the reconstructed pore. The eigenvalues of the co-variance matrix represent the principal axis lengths of the fitted ellipsoid, and the eigenvectors

represent the orientation of the principal axes. In the equation for a general ellipsoid,

$$\frac{x_0^2}{a^2} + \frac{y_0^2}{b^2} + \frac{z_0^2}{c^2} = 1 \quad (1)$$

where x_0 , y_0 , and z_0 are the local coordinate axes for the ellipsoid, the principal major semi-axis lengths, in decreasing order, are defined as a , b , and c . Note the local coordinate axes for the ellipsoid are distinguished from the global coordinate axes used in the general XCT analysis because the ellipsoid may be oriented such that the principal axes are not aligned with the global coordinate system. Using a fitted ellipsoid, the characteristic length of the pore would then be defined as the major axis length, defined as $2a$. This definition is more flexible for determining the characteristic length of flaws that are not spherical in shape.

In addition, the ratio of the principal axis lengths provide information on the *shape* of the flaw. For instance, if the major axis length is much larger than the minor and intermediate axis lengths ($a \gg b \approx c$) then the pore shape is needle-like (example shown later in Figure 4(A) when discussing shape results). It is important to note that the digital representation of pores by discrete cubic voxels can bias the morphology of the reconstructed pore, especially when the pore is resolved by a small number of voxels. When the pore size is similar to the voxel size, the pore shape cannot be adequately represented. Therefore, a volume cut-off of 125 voxels was used in this paper to filter pores for morphology analysis to ensure only resolvable pore morphologies are included in the analysis. This limit is consistent with those used in the literature [18, 27]. **Note that the methods in this paper were developed for convex pores or inclusions, which may be reasonably approximated by ellipsoidal representation. Failure in other materials may be controlled by defects at different scales (e.g. dislocations[32] or stacking faults[33]), which currently cannot be imaged using XCT, or defects of different morphologies (e.g. closed cracks), which require different representations, and so the methods in this paper may not be transferable to those**

205 **systems.**

2.2.4. *Microstructural Anisotropy*

Anisotropy in the microstructure has been shown to develop in sintered ceramics[34, 35, 36], and it can have an effect on anisotropy in mechanical properties[37]. Microstructural anisotropy can arise from preferred directional-
210 ity in the (i) pore *orientation* and (ii) *spatial distribution* of pores. The first type of anisotropy refers to the orientation of *individual* pores, and it can be characterized by the orientation of the major axis of the fitted ellipsoid. Preferred directionality in pore orientation can be detected by examining the distribu-
215 tion of major axis orientation for all pores. The second type of anisotropy refers to banded dispersions, in which pores exhibit tighter spacing in a specific direction[38, 39]. This type of anisotropy can be identified by examining the angle between nearest neighbor pores. The orientation between nearest neighbors is characterized by the vector that joins the centroids of nearest neighbor pores. For a set of pores that are isotropically distributed, all angles should
220 be equally likely, but certain angles are expected to dominate for banded or aligned dispersions. Using these methods, anisotropy in the microstructure can be quantified through XCT and linked to mechanical property anisotropy.

2.2.5. *Spatial Distribution of Pores*

The study of the spatial distribution of defects, including investigating the
225 nearest neighbor spacing between defects, is motivated by the role of inter-defect spacings on fragmentation[5, 7], strain-rate dependency[40, 41], and strength[21] in advanced ceramics. Characterization of spatial distributions may also shed light on the formation of process-induced defects and links to manufacturing parameters. The spatial distribution of defects is commonly characterized by
230 scalar metrics such as number density or volume fraction. Defect density can be quantified through XCT reconstructions by taking the number of defects identified through connected components analysis and dividing by the total reconstructed voxel volume. Volume fraction, or in this case, porosity, can be

quantified by considering the ratio of foreground voxels, which represent pore
 235 volume, to the total number of voxels, which represent the total sample volume.
 However, these scalar metrics do not provide any information on the type of
 spatial distribution observed, nor do they account for local variations in spacing.
 For example, while a random distribution of defects may share the same global
 density as a clustered distribution, local defect density will differ dramatically.

240 Such fluctuations in defect spacing have been linked to an increased variability
 in compressive strength in brittle materials[21], as well as a greater
 dependence on porosity for strength and stiffness[42]. Ultimately, density is
 an indirect and limited measure of defect spacing. With access to the spatial
 coordinates of individual defects through XCT reconstructions, deeper spatial
 245 analysis is possible. This section will outline nearest neighbor and tessellation
 methods for analyzing spatial relationships.

Nearest neighbor distance distributions have been used to classify the type
 of spatial distribution observed in inhomogeneous microstructures[39, 43, 44].
 This classification is based on comparisons between the observed nearest neigh-
 250 bor distribution and that of a Poisson process. Using reconstructed XCT data,
 the observed nearest neighbor distance between pores can be computed by tak-
 ing the distance between the centroidal coordinates of a pore and its nearest
 neighbor. The Poisson process models a randomly located distribution of points
 in which the location of each point is independent of the locations of all other
 255 points. Two ratios are used to classify the observed distribution:

$$Q = \frac{\bar{r}}{E(\bar{r})} \quad (2)$$

$$R = \frac{s^2}{E(s^2)} \quad (3)$$

where \bar{r} and s^2 are the mean and variance of the nearest neighbor distance for
 the observed pores, and $E(\bar{r})$ and $E(s^2)$ are the expected mean and variance of
 the nearest neighbor distance for the Poisson process. Physically, the Q and R
 ratios quantify the deviation of the observed nearest neighbor spacing from that

260 of a random distribution. To obtain the expected mean and variance in nearest neighbor distance for a three-dimensional Poisson process for comparison, the following analytical expressions have been developed [19, 39, 43]:

$$E(\bar{r}) = 0.893 \left(\frac{3V}{4\pi N} \right)^{\frac{1}{3}} \quad (4)$$

$$E(s^2) = 0.105 \left(\frac{4V}{3\pi N} \right)^{\frac{2}{3}} \quad (5)$$

where N is the number of points and V is the volume of the region of interest. The following guidelines for interpreting the two ratios have been given by 265 Bansal and Ardell[44] as:

$Q \approx 1, R \approx 1$: random distribution

$Q > 1, R \ll 1$: regular distribution

$Q < 1, R < 1$: clustered distribution

$Q < 1, R > 1$: clusters in a random background distribution

270 Note that the Poisson distribution models points while the observed defects have finite volume. As the size and volume fraction of the defects increase, the defect spacing will naturally deviate from that of a point distribution. Therefore, the above criteria are only valid for small pores with volume fractions less than 5% [44]. The pores in alumina under analysis in this paper were found to have 275 volume fractions of approximately $4.1 \pm 0.1\%$ on average, so the comparison is valid. The data that is generated through this analysis will be used to characterize the global defect distribution pattern in AD85 alumina. For materials where the secondary phase particles are present in higher volume fractions, the spacing comparison can be made against randomly simulated microstructures 280 with the same size distribution, like in Yang et al.[45].

Local spatial characteristics in AD85 microstructure can be analyzed through Voronoi tessellation. Voronoi tessellation has been used to analyze spatial distributions in many applications, including astronomy[46], biology[47], and ecology[48]. In terms of material science, Voronoi tessellation has been applied 285 to investigate the spatial distributions of particle reinforcements in composites[43,

45] and defects in metals[19, 20, 39]. Given a set of points in a volume, Voronoi tessellation is a method for discretizing the volume into polyhedrons, where the geometry of the polyhedrons are determined based on the distances between points. Each discretized polyhedron, known as a Voronoi cell, envelopes one
290 point. The faces of the cell are made up of planes bisecting the shortest lines between adjacent points such that each cell contains the space that is closest to its associated point than any other point. To apply this method using XCT data, the centroids of the reconstructed pores can be used as seed points for generating a tessellation. The geometry of the cells also define unique near
295 neighbors for each pore; cells sharing faces are counted as near neighbors, and each pore is therefore surrounded by a finite set of uniquely defined neighbors. The strength of this method is that it extracts spatial information for each individual pore, including cell volume, local volume fraction (ratio of pore volume to cell volume), mean near neighbor distance, and number of near neighbors.
300 As a result of each pore being associated with a cell, spatial properties of the Voronoi cell can be linked to the characteristics of the individual pore, such as size, shape, or orientation.

2.3. Mechanical Testing

Quasi-static uniaxial compression experiments were performed using a Ma-
305 terial Testing System (MTS) 810 load frame. The specimens were compressed along the longest dimension (3.5 mm). Loading was carried out using displacement control at a constant rate of 3.5×10^{-3} mm/s, which corresponds to a nominal strain rate of 1×10^{-3} s⁻¹. However the actual strain rate is approximately an order of magnitude lower owing to the compliance of the load frame,
310 and this is known for these experiments because digital image correlation was used to explore strain in the sample (methods presented later). Due to the high hardness of alumina, the specimens can indent into the load frame's compression platens under loading, leading to a non-uniform stress distribution. To prevent indentation and provide a hard surface for uniform stress distribution, tungsten
315 carbide platens jacketed in titanium were inserted between the specimen and the

load frame’s compression platens. The specimen and tungsten carbide platen interfaces were lubricated with high-pressure grease to allow for free lateral expansion during loading. A Promon U750 high speed camera capturing 630 by 750 pixels at 100 frames per second (FPS) was used to visualize the sample surface during the quasi-static compression experiments.

Dynamic compression experiments were performed on a Kolsky bar apparatus. The incident and transmitted bars were made of maraging steel with a stiffness of 200 GPa and a density of 8100 kg/m³. All bars were 12.7 mm in diameter. Again, tungsten carbide platens jacketed in titanium were used to protect the bars from indentation, and specimen-platen interfaces were lubricated with high pressure grease to allow for free lateral expansion. Note that the tungsten carbide platens are impedance matched to the incident and transmitted bars to minimize wave reflections at interfaces. The triangular incident pulse was created using a cylindrical maraging steel striker 304 mm in length in conjunction with a tin pulse shaper measuring 3.175 mm in diameter and 1 mm in thickness. This provided a rise time of 230 μ s and we found that good stress-equilibrium was obtained in our specimens (discussed later in Figure 7(A)). The surface of the specimen was visualized using a Shimadzu HPV-X2 ultra-high-speed camera recording at 500,000 FPS with a 1000 ns exposure time. In total, 128 frames spanning 400 x 250 pixels were captured for each experiment. At these frame rates, we were able to capture failure and post-peak fragmentation process.

Digital image correlation (DIC) was applied to in-situ recordings of experiments to obtain deformation measurements on specimens in quasi-static and dynamic compression experiments. DIC is a computer vision method that tracks speckle patterns on surfaces to compute deformation fields. The two-dimensional DIC technique is well established and has been applied to study the behaviour of a variety of materials (e.g., composites[49], aluminum foams[50], and mild steels[51]). See Pan et al.[52] and Dong et al.[53] for discussions on DIC theory and experimental design. Due to the small size of the specimens in this study, it was challenging to produce a speckle pattern suitable for DIC

measurements. Conventional methods such as commercial spray can paints or rollers produce speckles that are too coarse for samples of this size. An airbrush with a 0.15 mm nozzle set capable of producing speckles with diameters on the order of microns was found to generate a sufficiently fine speckle pattern (i.e. 5-10 pixels per speckle). One of the challenges to capturing at high frame rates, as required for capturing the dynamic experiments in this study, is producing adequate illumination on the specimen surface for low exposure times. To increase the reflectivity of the specimen surface, high gloss metallic paint was used to create the speckle pattern (see Figure 1(B)). In addition, a ring light consisting of a high power LED array from REL Inc. was used to provide increased illumination on the specimen surface. DIC analysis was performed using the commercial software VIC-2D (v6 2018) from Correlated Solutions (Irmo, South Carolina, US). The region of interest was discretized into 27 x 27 pixel subsets with a step size of 7 pixels. Correlation analysis was carried out using the zero-normalized sum of squared differences correlation criterion and the optimized 8-tap interpolation scheme[54]. Strains were computed from the displacement fields using the engineering strain tensor. The computed strain histories were matched to the stress histories to produce stress-strain curves. Quasi-static stress information was obtained from the load cell in the MTS load frame. Dynamic stress information was obtained using the transmitted bar strain gauge signal using:

$$\sigma(t) = E \frac{A_0}{A_B} \epsilon_T(t) \quad (6)$$

where σ is the stress (Pa) in the specimen, t is time (s), E is the Young's Modulus (Pa) of the transmitted bar, A_0 is the specimen cross-sectional area (m^2), A_B is the transmitted bar area (m^2), and $\epsilon_T(t)$ is the strain from the transmitted gauge.

3. Experimental Results

3.1. Pore Size Distribution

First we begin by presenting the pore size distribution in AD85 alumina. Shown in Figure 3(A) is the cumulative distribution of the pore size for 10 samples that eventually were tested in both quasi-static and dynamic compression experiments. For a given major axis length, the cumulative distribution defines the probability that the pore size is less than or equal to that major axis length. In this study, the cumulative distribution was computed empirically using:

$$F(l) = \frac{1}{n} \sum_{i=1}^n I(l_i \leq l) \quad (7)$$

where l is the major axis length, l_i is the total distribution of major axis lengths, n is the total number of of pores, and $F(l)$ is the empirical cumulative distribution function, which approximates the true cumulative distribution function for large n . The function I has a value of 1 when $l_i \leq l$, and 0 otherwise. Used in combination with the summation, I indicates the number of pores with a major axis length less than than l . In total, there are between 16,540 and 19,091 pores reconstructed for each sample in this study. The large number of pores quantified in this study is a key advantage of XCT analysis when compared the 565[55] or 1000[13] pores that are characterized through SEM or optical microscopy in other alumina studies. Given the large number of pores observed, the empirical cumulative distribution function is a good approximation of the theoretical distribution. From Figure 3(A), we observe that the pore size distribution remains mostly constant across all 10 samples, with median (50th percentile) values ranging from 16.0 μm to 17.2 μm . In all cases, pores smaller than 36.5 μm represent more than 90% of the defect population. Beyond 70 μm , the distribution ends in a long tail, indicating reduced frequency for larger defects. The largest pores in each sample range from 148 to 367 μm , which are 10-25 times larger than the median pore size. The distribution is therefore dominated by smaller pores, and large pores are infrequent. Overall, the pore size distribution is well

controlled in AD85 alumina, especially considering that the samples come from
400 different locations across multiple tiles.

3.2. Pore Morphology

To characterize pore morphology, we analyze the principal axis lengths of the fitted ellipsoids. The intermediate axis lengths of the fitted ellipsoids are plotted against the corresponding minor axis lengths for sample AD85 01 in
405 Figure 4(B). These results are similar for other samples considered in this study. Both lengths are normalized by the major axis length. The contour represents normalized frequency, with warmer colors representing higher frequency and cooler colors representing lower frequency. The ratios of the two normalized lengths serve as useful descriptors of the shape of the ellipsoid. Points that fall
410 on the diagonal line are pores with equal intermediate and minor axis lengths. Therefore, the upper right corner characterizes spherical pores ($a=b=c$), and the bottom left corner characterizes high aspect ratio, needle-like pores ($a \gg b \approx c$). Flat disc-like pores, in which the major and intermediate axes are much longer than the minor axis ($a \approx b \gg c$), are represented by the upper left corner of the
415 plot. In the pore data set for AD85, few data points occupy this region of the plot, so the pores tend to be rounded rather than flat. All of the above limiting cases are shown schematically in Figure 4(A). The wide spread of the points in Figure 4(B) indicates that the pores can take on a wide range of shapes, while the concentration of points near the center shows that there is a preferred shape
420 for the pores. Based on the location of the high frequency region, the majority of pores are slightly prolate spheroids. To give a quantitative measure of the general pore shape, the center values of the normalized intermediate and minor axis lengths in the high frequency region are (0.73, 0.62) in Figure 4(B). This trend is observed consistently as the center normalized intermediate and minor
425 axis lengths are 0.75 ± 0.04 and 0.64 ± 0.05 for all ten samples.

3.3. Microstructural Anisotropy

The orientation between nearest neighbors and the angles of individual pores were examined to identify anisotropy in the microstructure. Orientation in 3D

is described using the two angles θ and ϕ (see Figure 5(A) for orientation definition). The orientation between nearest neighbors is shown in a normalized polar histogram in Figure 5(B). To show only unique angles, the θ distribution was collapsed to between 0° and 180° . The solid black line at 90° in the θ plane indicates the direction of the long dimension of specimen, which is parallel to the thickness of the tile from which the specimen is cut. Both the θ and ϕ distributions span the whole range of possible angles, showing that near neighbors can take on a variety of orientations. In the ϕ distribution, the frequency for most angular bins are between 1.7% and 2.4% of the total distribution, with no distinct preference amongst the angles for higher or lower frequencies. In the θ distribution, the majority of the angular bins that are less than 60° and greater than 120° exhibit frequencies at or below 2%, while angular bins between 60° and 120° consistently show frequencies above 2%. For a set of randomly distributed pores, all orientations between nearest neighbors should be equally likely. Therefore, it is expected that one third of the nearest neighbor pairs would have an orientation between 60° and 120° , however, 38.5% of the pores were found to have a θ angle between 60° and 120° . In terms of spacing, this shows that there is an increased frequency in nearest neighbors along the thickness of the tile. This preference is observed consistently in all 10 samples, which suggests that the anisotropy in spatial distribution is global in AD85 alumina. Because the exact manufacturing process for this material is not known, it is difficult to identify the cause of this anisotropy. However, based on comparisons of ultra-sonic characterization data in the literature, Chang et al.[56] have theorized that uniaxial forming processes, such as hot pressing, cold pressing, extrusion, or pressure casting, can induce anisotropic pore distributions in which the pore density is greater along the pressing direction. Other characterization studies have linked anisotropic grain growth in alumina to uniaxial pressure when elongated powder particles are used[34, 35], though none have directly characterized the pores. Ultimately, this anisotropy is expected to have little effect on the mechanical behaviour of the material, as the deviation from an isotropic distribution is small.

460 Figure 5(C) shows the normalized polar histogram for the major axis orientation for sample AD85 01. In both the ϕ and θ distributions, all angular bins have frequencies between 1.7% and 2.5%, with no clear preference for any set of angles. Based on these distributions, the major axes of pores in AD85 are determined to be oriented randomly. The processing that causes slight anisotropy in
465 the spatial distribution of pores does not appear to cause observable anisotropy in the orientation of individual pores.

3.4. Spatial Distribution of Pores

To assess the spatial distribution of pores, we first examine the nearest neighbor distribution. The nearest neighbor distance was found to be well represented
470 by a normal distribution with a mean spacing of 23.1 μm and a standard deviation of 4.2 μm . The low standard deviation shows that the nearest neighbor spacing is tightly controlled. Comparisons of the observed distribution against the spacing in the Poisson point distribution provided an average of $Q = 1.21 \pm 0.06$ and $R = 0.37 \pm 0.03$, respectively. This indicates that the mean spacing is greater than that of a random distribution while the observed variance
475 in spacing is much lower than that of a random distribution. Taken together, these parameters indicate that the defects are generally regularly distributed.

Beyond global patterns, Voronoi tessellation was applied to investigate local spatial characteristics in the microstructure. Figure 6(A) shows a scatter log-log
480 plot of Voronoi cell volume as a function of pore size. The contour indicates normalized frequency, with cooler colors indicating lower frequency and warmer colors indicating higher frequency. The cell volume, which can be thought of as the region of influence around a pore, is plotted against pore size to investigate the relationship between size and spacing. Between cell volumes of $1.8 \times 10^4 \mu\text{m}^3$
485 and $1 \times 10^5 \mu\text{m}^3$, there is a tight concentration of data points in Figure 6(A) for all pore sizes. The horizontal band in Figure 6(A), outlined by the dashed lines, indicates that the average spacing between defects is largely independent of size, and the consistent cell volume is in agreement with the regular distribution predicted by the nearest neighbor method. The scatter about the band is the

490 greatest near a pore size of $14\ \mu\text{m}$ and decreases gradually as pore size increases.
This shows that the spacing around pores becomes more regular as the pore
size increases. Of the pores that deviate from the band, most exhibit larger
cell volumes than those in the band. Since larger cell volumes represent pores
that are farther from near neighbors, this suggests that the sparser regions
495 are typically occupied by smaller defects, while the majority of defects exist in
higher density regions.

3.5. Mechanical Testing

A key advantage of DIC strain measurements is the access to spatial distribu-
tion of strains, which allows for evaluation of stress equilibrium and confirmation
500 of a good Kolsky bar experiment. Others have checked for stress equilibrium
by comparing the front face stress, computed using the incident and reflected
waves, to the rear face stress, computed using the transmitted wave[57]. To
illustrate the process of checking for stress equilibrium in our experiments, Fig-
ure 7(A) shows the stress and strain histories for a dynamic compression test
505 matched up in time. A range of strain profiles are shown, each representing a
different area of interest (AOI) on the surface of the sample as indicated by the
inset in Figure 7(A). The average strain history was computed by averaging the
strain over the entire surface, and this strain is used later in stress-strain plots
in Figure 8(A). The stress, computed from the transmitted bar signal, is a mea-
510 sure of the bulk response of the specimen, while the strains are computed from
only one surface, with more local measurements being accessible through DIC.
Therefore, while agreement between strain profiles from different regions is rep-
resentative of good equilibrium on the sample surface, agreement between the
normalized stress and strain curves in Figure 7(A) serves as a further indicator
515 of stress equilibrium in the sample. Greater agreement was found between the
different AOI's for the dynamic tests than for the quasi-static tests in this study.
One advantage of using smaller specimens is that the surface to volume ratio
increases, so the surfaces that are imaged during the compression experiments
are more representative of the bulk behaviour. In most dynamic tests, chipping

520 was observed at the edges and corners of the sample as the strain accumulated,
but typically the sample surface remained plane and nominally intact by the
time peak strain is reached. For the test shown in Figure 7(A), chipping occurs
at the top left corner of the sample, leading to a destabilization of the strain field
in AOI 1 at 180 to 200 μs . This is responsible for the fluctuations in the AOI
525 1 strain profile near the peak strain, and, in general, strain profiles deviate the
most near the peak strain. Following peak strain, the sample surface remains
plane and intact for up to 4 frames before significant cracking and fragmenta-
tion occurs. These framing rates therefore allow for some strain measurements
of the post-peak relaxation of the material.

530 The combined quasi-static and dynamic stress-strain curves across all ex-
periments are shown in Figure 8(A). The strain rates in all experiments were
computed using a linear fit of the strain-time profile obtained through DIC.
The strain rates ranged from 2.0 to $2.2 \times 10^{-4} \text{ s}^{-1}$ in the quasi-static experi-
ments and 6.8 to $8.9 \times 10^1 \text{ s}^{-1}$ in the dynamic experiments. The stiffness was
535 obtained by taking the slope of the stress-strain curves. Table 2 shows the peak
compressive strength, stiffness, and failure strain for all experiments. In this
study, the quasi-static strength was found to be 2.24 ± 0.23 GPa. Arrowood
and Lankford[5] have reported a similar compressive strength of 2.14 GPa for
cylindrical AD85 specimens of a comparable size (6.36 mm diameter by 13.36
540 mm in length) tested at a strain rate of $1.1 \times 10^{-4} \text{ s}^{-1}$. With the increase in
strain rate in the dynamic tests, the compressive strength increases to 3.04
 ± 0.16 GPa, and the failure strain also increases from $1.01 \pm 0.10\%$ at quasi-
static to $1.29 \pm 0.05\%$ in the dynamic tests. This rate-dependent behaviour is
well documented in ceramics[58, 59]. The stiffness was measured to be 224 ± 12
545 GPa in the quasi-static tests and 235 ± 6 GPa in the dynamic tests. Though
the loading technique is slightly different between the two rates, the stiffness is
consistent within scatter. Both the strength and stiffness are comparable to the
manufacturer values in Table 1.

To quantify the variation across the two strain rates, we examine the coef-
550 ficient of variation (COV), a relative measure of variation which is defined as

the ratio of the standard deviation to the mean. Summarized in Table 2, the COV for stiffness, strength, and failure strain are 5.30%, 10.28%, and 10.30% in the quasi-static tests. The corresponding COV values are 2.54%, 5.20%, and 4.17% in the dynamic tests. The low COV values show relatively low variability in the mechanical properties. In general, it was found that greater peak stress corresponded to greater stress equilibrium in the specimen, which points to one source of variability in the mechanical results. Comparing the variability in properties between two strain rates, it can be seen that the COV values in the dynamic tests are roughly 50% lower than those in the quasi-static regime. The implications of these results are discussed next.

4. Discussion

This paper presents microstructural and mechanical characterization results on AD85 alumina, focusing on variability in the internal pore distribution and mechanical properties. Meso-scale internal pores were visualized using XCT, and a number of methods for interpreting 3D digital reconstructions have been applied to characterize the pore distribution. The mechanical response of the scanned material has been probed at quasi-static and dynamic rates. In the discussion section, we explore the microstructural characterization methods and their applications in the context of manufacturing and computational model parameters, then we assess the variability observed in the AD85 microstructure and uniaxial compression results.

4.1. Manufacturing

This study contributes to a growing body of work focused on the utilization of XCT as a 3D quantitative characterization tool[16, 18]. While spatial and contrast resolution in XCT have advanced to allow for the *visualization* of microstructural features, *characterization* requires methods for interpreting the reconstructed 3D data. The methodology presented in this paper can be applied to characterize pores or secondary phase particles in a range of materials, including composites, advanced ceramics, foams, and certain metal alloys.

580 In all of these materials, it is important to control the spatial heterogeneity
in the microstructure for the development of enhanced mechanical properties.
The XCT spatial characterization methods presented serve as powerful indica-
tors of spatial heterogeneity, allowing for the characterization of the type of
spatial distribution as well as the extent of variability in spacing. Using these
585 methods, manufacturing parameters or processes can be linked to the spatial
characteristics of the resulting microstructure. Since XCT is non-destructive,
manufacturing parameters and spatial distributions can further be linked to
mechanical properties of the characterized material, ultimately enhancing our
understanding of the relationships between processing, structure, and property.

590 As an example, consider the regularity in pore spacing found in AD85. X-
ray diffraction analysis of AD85 performed by the authors in Sano et al.[23] has
identified Mg_2SiO_4 as a secondary phase in the microstructure, which indicates
that magnesia and silica were introduced as additives during sintering. Gavrilov
et al.[60] investigated the microstructure of alumina co-doped by magnesia and
595 silica and linked Si/Mg ratios less than unity to greater uniformity in the mi-
crostructure. These findings, based on qualitative analysis of SEM images of
the microstructure in the Gavrilov study[60], are consistent with the spatial ho-
mogeneity characterized in the alumina in the present study. Using the R and
Q parameters from nearest neighbor comparisons and Voronoi tessellation, not
600 only can we confirm uniformity in the microstructure, but we can also quan-
tify the *degree* of uniformity relating to, for example, different ratios of Si/Mg.
This example shows how the XCT characterization methods presented can be
utilized in the optimization of processing parameters for the manufacturing of
materials.

605 4.2. Parameters for Computational Models

Recent studies are making efforts towards introducing distributions of defect
characteristics where computational models describing the properties or failure
of porous materials have traditionally employed single parameter defect charac-
teristics such as average defect size or defect density. Paliwal and Ramesh[61]

610 incorporated flaw size and orientation distributions in their model for inter-
acting flaws. Graham-Brady[21] investigated the use of Monte-Carlo simula-
tions as a method for introducing spatial variability into failure models. Levy
and Molinari[12] implicitly modeled variability in microstructure by assigning
fracture activation thresholds from different probability distributions to the de-
615 fect population. However, despite theoretical efforts to incorporate variability
and distributions of microstructural characteristics, experimental observations
of these characteristics are limited in the literature, and simulations in the above
studies are commonly performed using assumed or idealized distributions. The
characterization methods and results presented in this study are aimed at filling
620 this gap in characterization data, particularly for the characteristics that have
received little attention, such as defect spacing and morphology. Where density
is a limited representation of defect spacing, the Voronoi tessellation method pre-
sented provides direct measurements of distributions of average spacing around
individual pores. Ellipsoid representation allows for the quantification of pore
625 morphology as well as orientation (via major axis orientation) and size distri-
butions. Since all of these characterization tools can be applied simultaneously
to the reconstructed defects, multiple characteristics can be assigned to an indi-
vidual pore (i.e., it is possible to know the size, shape, orientation, and average
spacing around a given pore). Therefore, defect characteristics no longer form
630 disjointed descriptions of a single defect population. Instead, the various char-
acteristic distributions that describe a defect population can be incorporated
wholesale, and links between characteristics can be analyzed. As an example,
the Voronoi tessellation results for AD85 (Figure 6(A)) has shown that larger
pores typically occur in denser regions while smaller defects experience greater
635 variability in spacing. When incorporated into a model, these relationships
provide a higher fidelity representation of the true microstructure than general
characteristics.

4.3. Variability in Microstructure and Properties

XCT analysis in this study has shown that modern advanced ceramics can
640 be produced with very consistent microstructures. The microstructure of the
material under investigation has shown low variability across a range of charac-
terization parameters based on pore size, spatial distribution, orientation, and
morphology. The pore size distributions shown in Figure 3(A) are nearly iden-
tical across all specimens, with median pore size values ranging from 16.0 μm to
645 17.2 μm across ten samples, and so the defect size is well-controlled. In terms
of spacing, the coefficient of variation for the mean nearest neighbor distance,
computed using ten specimens, was found to be 5.7%, indicating low variation
in interpore spacing. Nearest neighbor classification based on the R and Q pa-
rameters also consistently indicated regular spacing across all samples. Other
650 qualitative characteristics such as the preferred orientation in nearest neighbors
and the prolate spheroidal morphology of pores have been repeatably observed
in multiple samples. The low variability observed in the microstructure suggests
that the mechanical properties should also exhibit low variability. In particular,
given the regularity in pore spacing, and therefore the absence of pore clustering,
655 the scatter in strength is expected to be low. The low coefficients of variation
for strength, failure strain, and stiffness in this study confirm that there is a
low level of mechanical variability across the 10 specimens, although there is a
difference in variability at the quasi-static and dynamic strain rates.

The discrepancy in the mechanical variability between the two strain rates
660 may in part be attributed to variability in testing conditions (e.g. misalignment
of platens). Adams and Sine[62] have emphasized that for advanced ceramics,
where the tensile strength is much lower than the compressive strength, mi-
nor deviations from parallel loading can introduce tensile stresses that cause
the specimen to fail well before the compressive strength is reached. More
665 recently, Swab et al.[63] showed that significantly higher quasi-static strength
values than are typically reported for boron carbide can be obtained through
the use of dumbbell shaped specimens in well-controlled experiments. While
all the tests were conducted using identically processed specimens, the paral-

670 lelism or coaxial alignment of the platens in the MTS load frame used in the
quasi-static experiments are different than those of the incident and transmitted
bars in the dynamic experiments. Analysis of the strain fields obtained through
DIC revealed that the level of stress equilibrium in the sample varies from test
to test, and in general, specimens that reached greater peak stress tended to
exhibit a higher level of agreement between strain profiles obtained from dif-
675 ferent regions. This may partially explain the lower variability observed in the
dynamic tests, as the stress equilibrium in the dynamic experiments was found
to be qualitatively superior than in the quasi-static experiments.

At the same time, the mechanism that is responsible for the rate-dependence
of strength in ceramics may also contribute to the difference in variability be-
680 tween the two strain rates. For brittle materials under compression at quasi-
static rates, it is often noted that failure is caused by the activation and growth of
micro-cracks from the "weakest link" defect[64, 65]. Typically, the critical defect
is assumed to be the largest defect in the specimen because the stress required
to initiate a micro-crack decreases with increasing defect size. During dynamic
685 compression, the high loading rate may exceed the growth rate of the micro-
crack from the critical defect, and as a result, a greater proportion of the defect
population may be activated[66, 67]. The growth and interaction of the total set
of micro-cracks eventually lead to macroscopic failure of the specimen[61, 68].
Therefore, while quasi-static failure is thought to be controlled by the size of
690 the critical defect, dynamic failure may have a greater dependence on the over-
all defect distribution. Based on the XCT measurements of pore size in the
present study, even though the size distributions are similar across all samples,
the extreme ends of the size distribution can vary significantly. The maximum
pore size in the 10 specimens were found to range from 148 to 367 μm , so the
695 largest pore quantified in one specimen may be over 50% larger than the largest
pore in another specimen. Consequently, the larger scatter in the quasi-static
properties may in part be explained by the greater variation in the maximum
defect size in the samples, while the lower variability in the dynamic properties
may be attributed to the consistent pore size distribution for sizes less than

700 36.5 μm across all samples.

5. Conclusion

Defect characterization is central to the development of improved advanced ceramics. In the present study, XCT and DIC were used to explore the microstructure and mechanical response of AD85 alumina. The microstructure
705 was found to be consistent across multiple characterization parameters based on pore size, spatial distribution, orientation, and morphology. Spatial analysis methods based on nearest neighbors and Voronoi tessellation were applied to characterize the inter-pore spacing as highly regular and size independent. The characterization methods and results presented can be applied in the design of
710 tailored ceramic microstructures and as improved computational model inputs. Uniaxial compression tests were performed to characterize the mechanical response of AD85, and the variability in the mechanical properties was found to be greater at quasi-static rates than at dynamic rates. The lower variability in the dynamic mechanical properties is attributed to the greater equilibrium
715 achieved in the Kolsky bar tests as well as to the activation of a greater number of pores during loading.

6. Acknowledgment

This research was sponsored by the Army Research Laboratory and was accomplished under Cooperative Agreement Number W911NF-12-2-0022. The
720 views and conclusions contained in this document are those of the authors and should not be interpreted as representing the official policies, either expressed or implied, of the Army Research Laboratory or the U.S. Government. The U.S. Government is authorized to reproduce and distribute reprints for Government purposes notwithstanding any copyright notation herein. The authors would
725 also like to express their thanks to Bernie Faulkner, Rick Bubenko, Haoyang Li, and Kapil Bhagavathula for their help in conducting the experiments.

Research described in this paper was performed at the BMIT facility at the Canadian Light Source, which is supported by the Canada Foundation for Innovation, Natural Sciences and Engineering Research Council of Canada, the University of Saskatchewan, the Government of Saskatchewan, Western Economic Diversification Canada, the National Research Council Canada, and the Canadian Institutes of Health Research. We acknowledge Sergei Gasilov and Ning Zhu for their help in obtaining and reconstructing the XCT scans.

7. Data availability

735 The raw/processed data required to reproduce these findings cannot be
shared at this time as the data also forms part of an ongoing study.

References

- [1] W. W. Chen, A. M. Rajendran, B. Song, X. Nie, Dynamic fracture of
ceramics in armor applications, *Journal of the American Ceramic So-*
740 *ciety* 90 (4) 1005–1018. arXiv:<https://ceramics.onlinelibrary.wiley.com/doi/pdf/10.1111/j.1551-2916.2007.01515.x>, doi:
10.1111/j.1551-2916.2007.01515.x.
URL <https://ceramics.onlinelibrary.wiley.com/doi/abs/10.1111/j.1551-2916.2007.01515.x>
- [2] S.-T. Buljan, S. Wayne, Wear and design of ceramic cutting
745 tool materials, *Wear* 133 (2) (1989) 309 – 321. doi:[https://doi.org/10.1016/0043-1648\(89\)90044-6](https://doi.org/10.1016/0043-1648(89)90044-6).
URL <http://www.sciencedirect.com/science/article/pii/0043164889900446>
- [3] L. SEDEL, Evolution of alumina-on-alumina implants: A review, *Clinical*
750 *orthopaedics and related research* (379) (2000) 48–54.
- [4] J.-H. Park, Y.-H. Koh, H.-E. Kim, C. S. Hwang, E. S. Kang, Den-
sification and mechanical properties of titanium diboride with silicon
nitride as a sintering aid, *Journal of the American Ceramic Society*
755 82 (11) 3037–3042. arXiv:<https://ceramics.onlinelibrary.wiley.com/doi/pdf/10.1111/j.1151-2916.1999.tb02199.x>, doi:10.1111/j.1151-2916.1999.tb02199.x.
URL <https://ceramics.onlinelibrary.wiley.com/doi/abs/10.1111/j.1151-2916.1999.tb02199.x>

- 760 [5] R. Arrowood, J. Lankford, Compressive fracture processes in an alumina-glass composite, *Journal of Materials Science* 22 (10) (1987) 3737–3744. doi:10.1007/BF01161487. URL <https://doi.org/10.1007/BF01161487>
- [6] R. L. COBLE, W. D. KINGERY, Effect of porosity on physical properties of sintered alumina, *Journal of the American Ceramic Society* 39 (11) 377–385. arXiv:<https://ceramics.onlinelibrary.wiley.com/doi/pdf/10.1111/j.1151-2916.1956.tb15608.x>, doi:10.1111/j.1151-2916.1956.tb15608.x. URL <https://ceramics.onlinelibrary.wiley.com/doi/abs/10.1111/j.1151-2916.1956.tb15608.x>
- 770 [7] J. D. Hogan, L. Farbaniec, T. Sano, M. Shaeffer, K. Ramesh, The effects of defects on the uniaxial compressive strength and failure of an advanced ceramic, *Acta Materialia* 102 (2016) 263 – 272. doi:<https://doi.org/10.1016/j.actamat.2015.09.028>. URL <http://www.sciencedirect.com/science/article/pii/S1359645415007053>
- [8] S. C. CARNIGLIA, Working model for porosity effects on the uniaxial strength of ceramics, *Journal of the American Ceramic Society* 55 (12) 610–618. arXiv:<https://ceramics.onlinelibrary.wiley.com/doi/pdf/10.1111/j.1151-2916.1972.tb13454.x>, doi:10.1111/j.1151-2916.1972.tb13454.x. URL <https://ceramics.onlinelibrary.wiley.com/doi/abs/10.1111/j.1151-2916.1972.tb13454.x>
- 785 [9] N. Ramakrishnan, V. S. Arunachalam, Effective elastic moduli of porous ceramic materials, *Journal of the American Ceramic Society* 76 (11) 2745–2752. arXiv:<https://ceramics.onlinelibrary.wiley.com/doi/pdf/10.1111/j.1151-2916.1993.tb04011.x>, doi:10.1111/j.1151-2916.1993.tb04011.x.

URL <https://ceramics.onlinelibrary.wiley.com/doi/abs/10.1111/j.1151-2916.1993.tb04011.x>

790

- [10] G. Hu, J. Liu, L. Graham-Brady, K. Ramesh, A 3d mechanistic model for brittle materials containing evolving flaw distributions under dynamic multiaxial loading, *Journal of the Mechanics and Physics of Solids* 78 (2015) 269 – 297. doi:<https://doi.org/10.1016/j.jmps.2015.02.014>.

795

URL <http://www.sciencedirect.com/science/article/pii/S0022509615000459>

- [11] N. P. Daphalapurkar, K. Ramesh, L. Graham-Brady, J.-F. Molinari, Predicting variability in the dynamic failure strength of brittle materials considering pre-existing flaws, *Journal of the Mechanics and Physics of Solids* 59 (2) (2011) 297 – 319. doi:<https://doi.org/10.1016/j.jmps.2010.10.006>.

800

URL <http://www.sciencedirect.com/science/article/pii/S0022509610002218>

- [12] S. Levy, J. Molinari, Dynamic fragmentation of ceramics, signature of defects and scaling of fragment sizes, *Journal of the Mechanics and Physics of Solids* 58 (1) (2010) 12 – 26. doi:<https://doi.org/10.1016/j.jmps.2009.09.002>.

805

URL <http://www.sciencedirect.com/science/article/pii/S0022509609001380>

- [13] H. Abe, M. Naito, T. Hotta, N. Shinohara, K. Uematsu, Flaw size distribution in high-quality alumina, *Journal of the American Ceramic Society* 86 (6) 1019–1021. arXiv:<https://ceramics.onlinelibrary.wiley.com/doi/pdf/10.1111/j.1151-2916.2003.tb03411.x>, doi:10.1111/j.1151-2916.2003.tb03411.x.

810

URL <https://ceramics.onlinelibrary.wiley.com/doi/abs/10.1111/j.1151-2916.2003.tb03411.x>

- [14] N. Shinohara, M. Okumiya, T. Hotta, K. Nakahira, M. Naito, K. Uematsu, Morphological changes in process-related large pores of granular compacted and sintered alumina, *Journal of the American Ceramic Society* 83 (7) 1633–1640. arXiv:<https://ceramics.onlinelibrary.wiley.com/doi/pdf/10.1111/j.1151-2916.2000.tb01442.x>, doi:10.1111/j.1151-2916.2000.tb01442.x.
URL <https://ceramics.onlinelibrary.wiley.com/doi/abs/10.1111/j.1151-2916.2000.tb01442.x>
- [15] Y. Zhang, M. Inoue, N. Uchida, K. Uematsu, Characterization of processing pores and their relevance to the strength in alumina ceramics, *Journal of Materials Research* 14 (8) (1999) 3370–3374. doi:10.1557/JMR.1999.0456.
- [16] C. A. Moorehead, J. M. Sietins, J. J. Swab, Meso-scale microstructural agglomerate quantification in boron carbide using x-ray microcomputed tomography, *Materials Characterization* 141 (2018) 177 – 185. doi:<https://doi.org/10.1016/j.matchar.2018.04.053>.
URL <http://www.sciencedirect.com/science/article/pii/S1044580317332783>
- [17] J. N. Dastgerdi, A. Miettinen, J. Parkkonen, H. Remes, Multiscale microstructural characterization of particulate-reinforced composite with non-destructive x-ray micro- and nanotomography, *Composite Structures* 194 (2018) 292 – 301. doi:<https://doi.org/10.1016/j.compstruct.2018.04.022>.
URL <http://www.sciencedirect.com/science/article/pii/S0263822317328702>
- [18] S. Tammas-Williams, H. Zhao, F. Léonard, F. Derguti, I. Todd, P. Prangnell, Xct analysis of the influence of melt strategies on defect population in ti-6al-4v components manufactured by selective electron beam melting, *Materials Characterization* 102 (2015) 47 – 61.

doi:<https://doi.org/10.1016/j.matchar.2015.02.008>.

URL <http://www.sciencedirect.com/science/article/pii/S104458031500039X>

[19] M. Li, S. Ghosh, O. Richmond, H. Weiland, T. Rouns, Three dimensional characterization and modeling of particle reinforced metal matrix composites: part i: Quantitative description of microstructural morphology, *Materials Science and Engineering: A* 265 (1) (1999) 153 – 173.
850 doi:[https://doi.org/10.1016/S0921-5093\(98\)01132-0](https://doi.org/10.1016/S0921-5093(98)01132-0).

URL <http://www.sciencedirect.com/science/article/pii/S0921509398011320>
855

[20] M. Li, S. Ghosh, O. Richmond, H. Weiland, T. Rouns, Three dimensional characterization and modeling of particle reinforced metal matrix composites part ii: damage characterization, *Materials Science and Engineering: A* 266 (1) (1999) 221 – 240.
860 doi:[https://doi.org/10.1016/S0921-5093\(98\)01133-2](https://doi.org/10.1016/S0921-5093(98)01133-2).

URL <http://www.sciencedirect.com/science/article/pii/S0921509398011332>

[21] L. Graham-Brady, Statistical characterization of meso-scale uniaxial compressive strength in brittle materials with randomly occurring flaws, *International Journal of Solids and Structures* 47 (18) (2010) 2398 – 2413.
865 doi:<https://doi.org/10.1016/j.ijsolstr.2010.04.034>.

URL <http://www.sciencedirect.com/science/article/pii/S0020768310001708>

[22] Coorstek, Advanced alumina brochure, Brochure (2016).

870 URL <https://www.coorstek.com/media/1715/advanced-alumina-brochure.pdf>

[23] T. Sano, I. Buterbaugh, T. Walter, J. Catalano, B. Koch, C. Lo, J. Hogan, Correlation of microstructure to mechanical properties in two grades of alumina, in: B. Li, J. Li, S. Ikhmayies, M. Zhang, Y. E. Kalay, J. S.

- 875 Carpenter, J.-Y. Hwang, S. N. Monteiro, D. Firrao, A. Brown, C. Bai,
Z. Peng, J. P. Escobedo-Diaz, R. Goswami, J. Kim (Eds.), *Characterization
of Minerals, Metals, and Materials 2018*, Springer International Publishing,
Cham, 2018, pp. 75–81.
- [24] T. W. Wysokinski, D. Chapman, G. Adams, M. Renier, P. Suortti,
880 W. Thomlinson, Beamlines of the biomedical imaging and therapy
facility at the canadian light source—part 1, *Nuclear Instruments and
Methods in Physics Research Section A: Accelerators, Spectrometers,
Detectors and Associated Equipment* 582 (1) (2007) 73 – 76, proceedings
of the 14th National Conference on Synchrotron Radiation Research.
885 doi:<https://doi.org/10.1016/j.nima.2007.08.087>.
URL [http://www.sciencedirect.com/science/article/pii/
S0168900207017482](http://www.sciencedirect.com/science/article/pii/S0168900207017482)
- [25] K. V. Mardia, T. Hainsworth, A spatial thresholding method for image seg-
mentation, *IEEE transactions on pattern analysis and machine intelligence*
890 10 (6) (1988) 919–927.
- [26] E. Maire, P. J. Withers, Quantitative x-ray tomography, *International Ma-
terials Reviews* 59 (1) (2014) 1–43. arXiv:[https://doi.org/10.1179/
1743280413Y.0000000023](https://doi.org/10.1179/1743280413Y.0000000023), doi:10.1179/1743280413Y.0000000023.
URL <https://doi.org/10.1179/1743280413Y.0000000023>
- 895 [27] S. R. Stock, Recent advances in x-ray microtomography applied
to materials, *International Materials Reviews* 53 (3) (2008) 129–
181. arXiv:<https://doi.org/10.1179/174328008X277803>, doi:10.
1179/174328008X277803.
URL <https://doi.org/10.1179/174328008X277803>
- 900 [28] H. Horii, S. Nemat-Nasser, Compression-induced microcrack growth in brittle
solids: Axial splitting and shear failure, *Journal of Geophysical Re-
search: Solid Earth* 90 (B4) (1985) 3105–3125.

- [29] M. Kachanov, I. Tsukrov, B. Shafiro, Effective moduli of solids with cavities of various shapes, *Applied Mechanics Reviews* 47 (1S) (1994) S151–S174.
- 905 [30] A. P. Roberts, E. J. Garboczi, Elastic properties of model porous ceramics, *Journal of the American Ceramic Society* 83 (12) (2000) 3041–3048.
- [31] G. Bruno, M. Kachanov, Microstructure–property connections for porous ceramics: the possibilities offered by micromechanics, *Journal of the American Ceramic Society* 99 (12) (2016) 3829–3852.
- 910 [32] T. Mitchell, K. Lagerlöf, A. Heuer, Dislocations in ceramics, *Materials science and technology* 1 (11) (1985) 944–949.
- [33] H. Iwata, U. Lindelfelt, S. Öberg, P. Briddon, Stacking faults in silicon carbide, *Physica B: Condensed Matter* 340 (2003) 165–170.
- [34] A. Shui, N. Uchida, K. Uematsu, Origin of shrinkage anisotropy during sintering for uniaxially pressed alumina compacts, *Powder Technology* 127 (1) 9 – 18. doi:[https://doi.org/10.1016/S0032-5910\(02\)00004-9](https://doi.org/10.1016/S0032-5910(02)00004-9).
URL <http://www.sciencedirect.com/science/article/pii/S0032591002000049>
- 915 [35] A. Shui, M. Saito, N. Uchida, K. Uematsu, Development of anisotropic microstructure in uniaxially pressed alumina compacts, *Journal of the European Ceramic Society* 22 (8) (2002) 1217 – 1223. doi:[https://doi.org/10.1016/S0955-2219\(01\)00434-4](https://doi.org/10.1016/S0955-2219(01)00434-4).
URL <http://www.sciencedirect.com/science/article/pii/S0955221901004344>
- 920 [36] A. Zavaliangos, J. M. Missiaen, D. Bouvard, Anisotropy in shrinkage during sintering, *Science of Sintering* 38 (1) (2006) 13–25.
URL <https://hal.archives-ouvertes.fr/hal-00196207>
- [37] H. P. KIRCHNER, R. M. GRUVER, Strength-anisotropy-grain size relations in ceramic oxides, *Journal of the American Ceramic Society* 53 (5) 232–236. arXiv:<https://ceramics.onlinelibrary.wiley>.
- 930

com/doi/pdf/10.1111/j.1151-2916.1970.tb12083.x, doi:10.1111/j.
1151-2916.1970.tb12083.x.
URL [https://ceramics.onlinelibrary.wiley.com/doi/abs/10.1111/
j.1151-2916.1970.tb12083.x](https://ceramics.onlinelibrary.wiley.com/doi/abs/10.1111/j.1151-2916.1970.tb12083.x)

935 [38] H. F. Fischmeister, Applications of quantitative microscopy in materials
engineering, *Journal of Microscopy* 95 (1) 119–143. arXiv:[https://onlinelibrary.wiley.com/doi/pdf/10.1111/j.1365-2818.1972.
tb03715.x](https://onlinelibrary.wiley.com/doi/pdf/10.1111/j.1365-2818.1972.tb03715.x), doi:10.1111/j.1365-2818.1972.tb03715.x.
URL [https://onlinelibrary.wiley.com/doi/abs/10.1111/j.
1365-2818.1972.tb03715.x](https://onlinelibrary.wiley.com/doi/abs/10.1111/j.1365-2818.1972.tb03715.x)

[39] W. Spitzig, J. Kelly, O. Richmond, Quantitative characterization of
second-phase populations, *Metallography* 18 (3) (1985) 235 – 261.
doi:[https://doi.org/10.1016/0026-0800\(85\)90045-X](https://doi.org/10.1016/0026-0800(85)90045-X).
URL [http://www.sciencedirect.com/science/article/pii/
002608008590045X](http://www.sciencedirect.com/science/article/pii/S002608008590045X)

[40] S. Nemat-Nasser, H. Deng, Strain-rate effect on brittle failure in com-
pression, *Acta Metallurgica et Materialia* 42 (3) (1994) 1013 – 1024.
doi:[https://doi.org/10.1016/0956-7151\(94\)90295-X](https://doi.org/10.1016/0956-7151(94)90295-X).
URL [http://www.sciencedirect.com/science/article/pii/
095671519490295X](http://www.sciencedirect.com/science/article/pii/S095671519490295X)

[41] F. Zhou, J.-F. Molinari, K. Ramesh, A cohesive model based fragmen-
tation analysis: effects of strain rate and initial defects distribution,
International Journal of Solids and Structures 42 (18) (2005) 5181 – 5207.
doi:<https://doi.org/10.1016/j.ijsolstr.2005.02.009>.
955 URL [http://www.sciencedirect.com/science/article/pii/
S0020768305000624](http://www.sciencedirect.com/science/article/pii/S0020768305000624)

[42] R. Dorey, J. Yeomans, P. Smith, Effect of pore clustering on
the mechanical properties of ceramics, *Journal of the Euro-
pean Ceramic Society* 22 (4) (2002) 403 – 409. doi:[https://doi.org/10.1016/S0955-2006\(02\)00000-0](https://doi.org/10.1016/S0955-2006(02)00000-0)

- 960 //doi.org/10.1016/S0955-2219(01)00303-X.
URL <http://www.sciencedirect.com/science/article/pii/S095522190100303X>
- [43] R. Pyrz, Quantitative description of the microstructure of composites. part i: Morphology of unidirectional composite systems, Composites Science and Technology 50 (2) (1994) 197 – 208.
965 doi:[https://doi.org/10.1016/0266-3538\(94\)90141-4](https://doi.org/10.1016/0266-3538(94)90141-4).
URL <http://www.sciencedirect.com/science/article/pii/S0266353894901414>
- [44] P. Bansal, A. Ardell, Average nearest-neighbor distances between uniformly distributed finite particles, Metallography 5 (2) (1972) 97 – 111.
970 doi:[https://doi.org/10.1016/0026-0800\(72\)90048-1](https://doi.org/10.1016/0026-0800(72)90048-1).
URL <http://www.sciencedirect.com/science/article/pii/S0026080072900481>
- [45] N. Yang, J. Boselli, P. Gregson, I. Sinclair, Simulation and quantitative assessment of finitesize particle distributions in metal matrix composites, Materials Science and Technology 16 (7-8) (2000) 797–805.
975 arXiv:<https://doi.org/10.1179/026708300101508469>, doi:10.1179/026708300101508469.
URL <https://doi.org/10.1179/026708300101508469>
- 980 [46] M. Cappellari, Y. Copin, Adaptive spatial binning of integral-field spectroscopic data using Voronoi tessellations, Monthly Notices of the Royal Astronomical Society 342 (2) (2003) 345–354. arXiv:<http://oup.prod.sis.lan/mnras/article-pdf/342/2/345/3407404/342-2-345.pdf>, doi:10.1046/j.1365-8711.2003.06541.x.
985 URL <https://dx.doi.org/10.1046/j.1365-8711.2003.06541.x>
- [47] A. Poupon, Voronoi and voronoi-related tessellations in studies of protein structure and interaction, Current Opinion in Structural Biology 14 (2) (2004) 233 – 241. doi:<https://doi.org/10.1016/j.sbi.2004.03.010>.

- URL <http://www.sciencedirect.com/science/article/pii/S0959440X04000442>
990
- [48] N. C. Kenkel, Spatial Competition Models for Plant Populations, Springer Netherlands, Dordrecht, 1991, pp. 387–397. doi:10.1007/978-94-011-3418-7_34.
URL https://doi.org/10.1007/978-94-011-3418-7_34
- 995 [49] J.-N. Périé, S. Calloch, C. Cluzel, F. Hild, Analysis of a multiaxial test on a c/c composite by using digital image correlation and a damage model, Experimental Mechanics 42 (3) (2002) 318–328. doi:10.1007/BF02410989.
URL <https://doi.org/10.1007/BF02410989>
- [50] A.-F. Bastawros, H. Bart-Smith, A. Evans, Experimental analysis of
1000 deformation mechanisms in a closed-cell aluminum alloy foam, Journal of the Mechanics and Physics of Solids 48 (2) (2000) 301 – 322.
doi:[https://doi.org/10.1016/S0022-5096\(99\)00035-6](https://doi.org/10.1016/S0022-5096(99)00035-6).
URL <http://www.sciencedirect.com/science/article/pii/S0022509699000356>
- 1005 [51] B. Wattrisse, A. Chrysochoos, J.-M. Muracciole, M. Némoz-Gaillard, Analysis of strain localization during tensile tests by digital image correlation, Experimental Mechanics 41 (1) (2001) 29–39. doi:10.1007/BF02323101.
URL <https://doi.org/10.1007/BF02323101>
- [52] B. Pan, K. Qian, H. Xie, A. Asundi, Two-dimensional digital image correlation for in-plane displacement and strain measurement: a review, Measurement Science and Technology 20 (6) (2009) 062001.
1010 URL <http://stacks.iop.org/0957-0233/20/i=6/a=062001>
- [53] Y. Dong, B. Pan, A review of speckle pattern fabrication and assessment for digital image correlation, Experimental Mechanics 57 (8) (2017) 1161–
1015 1181. doi:10.1007/s11340-017-0283-1.
URL <https://doi.org/10.1007/s11340-017-0283-1>

- [54] H. W. Schreier, J. R. Braasch, M. A. Sutton, Systematic errors in digital image correlation caused by intensity interpolation, *Optical engineering* 39.
- [55] S. Nakamura, S. Tanaka, Z. Kato, K. Uematsu, Strength-processing defects relationship based on micrographic analysis and fracture mechanics in alumina ceramics, *Journal of the American Ceramic Society* 92 (3) 688–693. arXiv:<https://ceramics.onlinelibrary.wiley.com/doi/pdf/10.1111/j.1551-2916.2008.02904.x>, doi:10.1111/j.1551-2916.2008.02904.x.
1020
URL <https://ceramics.onlinelibrary.wiley.com/doi/abs/10.1111/j.1551-2916.2008.02904.x>
1025
- [56] L.-S. Chang, T.-H. Chuang, W. Wei, Characterization of alumina ceramics by ultrasonic testing, *Materials Characterization* 45 (3) (2000) 221 – 226. doi:[https://doi.org/10.1016/S1044-5803\(00\)00081-4](https://doi.org/10.1016/S1044-5803(00)00081-4).
1030
URL <http://www.sciencedirect.com/science/article/pii/S1044580300000814>
- [57] Wu, X. J., Gorham, D. A., Stress equilibrium in the split hopkinson pressure bar test, *J. Phys. IV France* 07 (1997) C3–91–C3–96. doi:10.1051/jp4:1997318.
1035
URL <https://doi.org/10.1051/jp4:1997318>
- [58] J. Lankford, Mechanisms responsible for strain-rate-dependent compressive strength in ceramic materials, *Journal of the American Ceramic Society* 64 (2) C-33–C-34. arXiv:<https://ceramics.onlinelibrary.wiley.com/doi/pdf/10.1111/j.1151-2916.1981.tb09570.x>, doi:10.1111/j.1151-2916.1981.tb09570.x.
1040
URL <https://ceramics.onlinelibrary.wiley.com/doi/abs/10.1111/j.1151-2916.1981.tb09570.x>
- [59] J. Lankford, High strain rate compression and plastic flow of ceramics, *Journal of Materials Science Letters* 15 (9) (1996) 745–750. doi:10.1007/

1045 BF00274593.
 URL <https://doi.org/10.1007/BF00274593>

[60] K. L. Gavrilov, S. J. Bennison, K. R. Mikeska, R. Levi-Setti, Role of magnesia and silica in alumina microstructure evolution, *Journal of Materials Science* 38 (19) (2003) 3965–3972. doi:10.1023/A:1026206414377.
 1050 URL <https://doi.org/10.1023/A:1026206414377>

[61] B. Paliwal, K. Ramesh, An interacting micro-crack damage model for failure of brittle materials under compression, *Journal of the Mechanics and Physics of Solids* 56 (3) (2008) 896 – 923. doi:<https://doi.org/10.1016/j.jmps.2007.06.012>.
 1055 URL <http://www.sciencedirect.com/science/article/pii/S0022509607001391>

[62] M. Adams, G. Sines, Methods for determining the strength of brittle materials in compressive stress states.

[63] J. J. Swab, C. S. Meredith, D. T. Casem, W. R. Gamble, Static and dynamic compression strength of hot-pressed boron carbide using a dumbbell-shaped specimen, *Journal of Materials Science* 52 (17) (2017) 10073–10084. doi:10.1007/s10853-017-1210-7.
 1060 URL <https://doi.org/10.1007/s10853-017-1210-7>

[64] W. Weibull, A statistical theory of strength of materials, Royal Swedish Institute for Engineering Research.
 1065

[65] W. Weibull, et al., A statistical distribution function of wide applicability, *Journal of applied mechanics* 18 (3) (1951) 293–297.

[66] J. Lankford Jr., The role of dynamic material properties in the performance of ceramic armor, *International Journal of Applied Ceramic Technology* 1 (3) 205–210. arXiv:<https://ceramics.onlinelibrary.wiley.com/doi/pdf/10.1111/j.1744-7402.2004.tb00171.x>, doi:10.1111/j.1744-7402.2004.tb00171.x.
 1070

URL <https://ceramics.onlinelibrary.wiley.com/doi/abs/10.1111/j.1744-7402.2004.tb00171.x>

- 1075 [67] K. Ravi-Chandar, W. G. Knauss, An experimental investigation into dynamic fracture: Iii. on steady-state crack propagation and crack branching, International Journal of Fracture 26 (2) (1984) 141–154. doi:10.1007/BF01157550.

URL <https://doi.org/10.1007/BF01157550>

- 1080 [68] B. Paliwal, K. Ramesh, Effect of crack growth dynamics on the rate-sensitive behavior of hot-pressed boron carbide, Scripta Materialia 57 (6) (2007) 481 – 484. doi:<https://doi.org/10.1016/j.scriptamat.2007.05.028>.

URL <http://www.sciencedirect.com/science/article/pii/S1359646207003892>

1085 S1359646207003892

List of Figures

	1	A) AD85 alumina sample dimensions with hot pressing direction along the long edge. B) Speckled sample under dynamic compression experiment lighting taken using the Shimadzu HPV-X2.	44
1090	2	Schematic of reconstruction process showing A) XCT scan of AD85 at 3 μm ; B) binary cross-sections of segmented pores; C) 3D rendering of reconstructed defects.	45
	3	Cumulative distribution function plot of the major axis length for all 10 AD85 samples.	45
1095	4	A) Examples of the limiting cases for AD85 pore shapes that can be presented using general ellipsoids. B) Intermediate axis length plotted against minor axis length. Both lengths are normalized by the major axis. Color bar shows normalized density.	46
1100	5	A) Spherical coordinate convention for orientation. B) AD85 nearest neighbor orientation polar histogram. C) AD85 pore major axis orientation polar histogram. The blue and orange represent the ϕ and θ distributions, respectively. The black line at 90° represents the long dimension of the sample.	46
1105	6	Log-log plot of Voronoi cell volume as a function of pore major axis length in AD85. Contour shows normalized density. Dashed lines indicate boundaries to the high frequency band where the majority of data points lie. The inset is a visualization of Voronoi tessellation where the red dots are seed points.	47
1110	7	Strain profiles from DIC are matched up to the stress profile computed from the transmitted gauge. The inset shows the area of interest (AOI) each strain profile is computed from. The red strain profile is the average of the entire face.	47
	8	Stress-strain curves for the quasi-static (solid line) and dynamic (dashed line) compression experiments of AD85 alumina.	48

1115 **List of Tables**

1	Material properties for AD85 alumina as reported by CoorsTek Inc.	49
2	Summary of stiffness, strength, and failure strain in quasi-static (QS) and dynamic (DYN) compression experiments with coeffi- cient of variation (COV)	50

1120

8. Figures

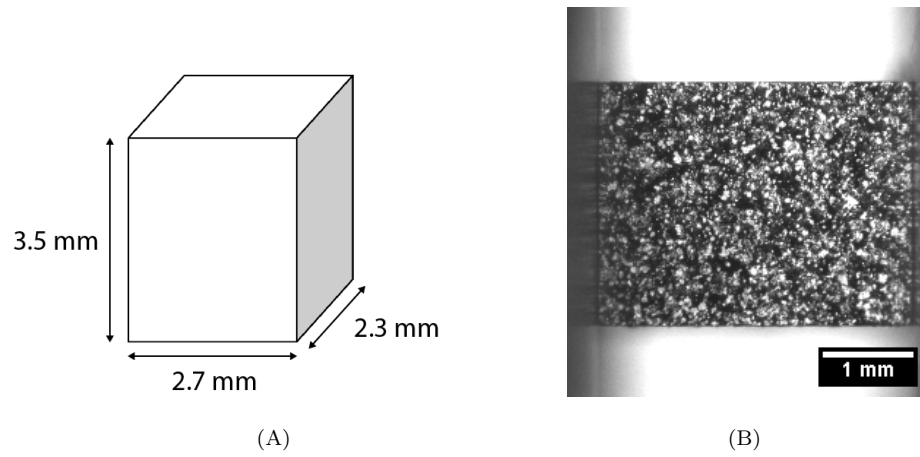


Figure 1: A) AD85 alumina sample dimensions with hot pressing direction along the long edge. B) Speckled sample under dynamic compression experiment lighting taken using the Shimadzu HPV-X2.

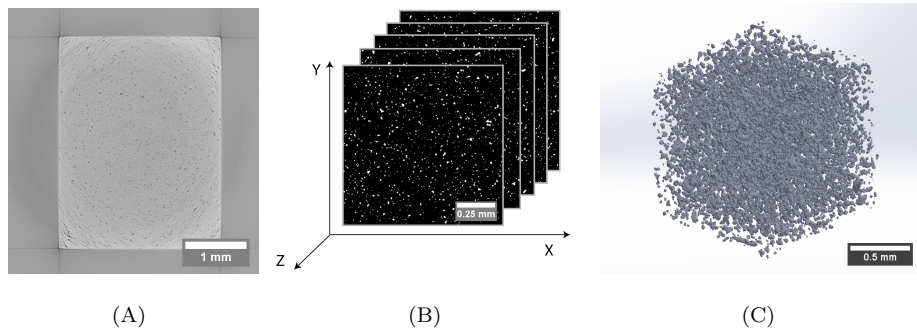


Figure 2: Schematic of reconstruction process showing A) XCT scan of AD85 at $3 \mu\text{m}$; B) binary cross-sections of segmented pores; C) 3D rendering of reconstructed defects.

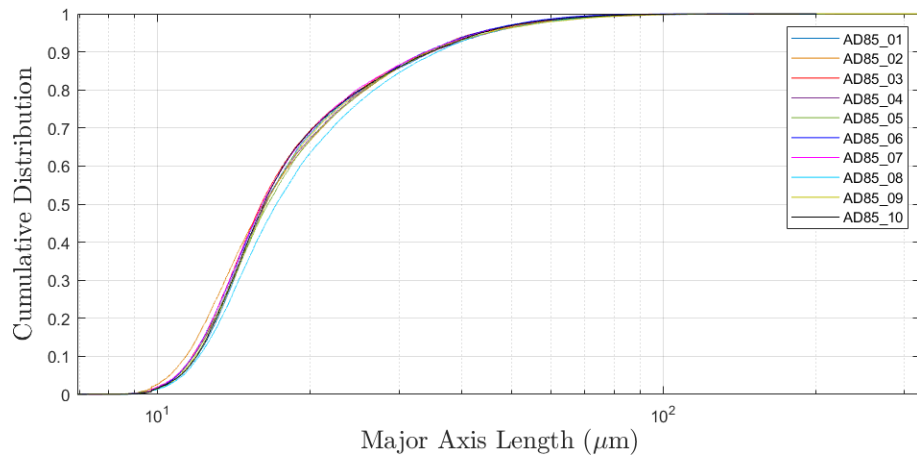


Figure 3: Cumulative distribution function plot of the major axis length for all 10 AD85 samples.

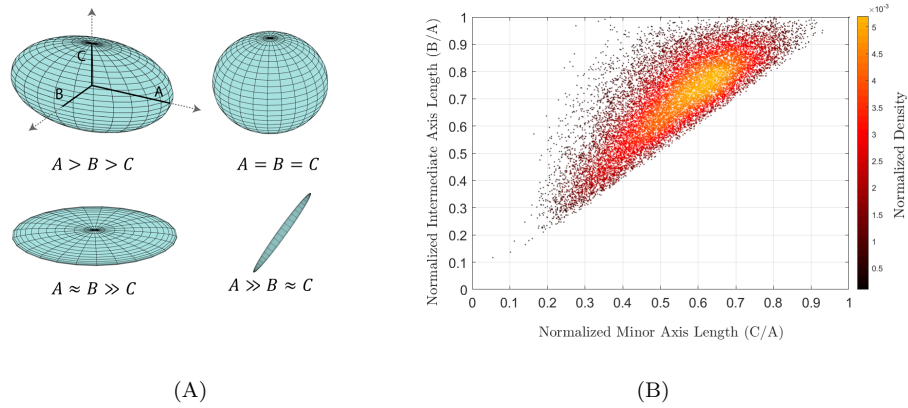


Figure 4: A) Examples of the limiting cases for AD85 pore shapes that can be presented using general ellipsoids. B) Intermediate axis length plotted against minor axis length. Both lengths are normalized by the major axis. Color bar shows normalized density.

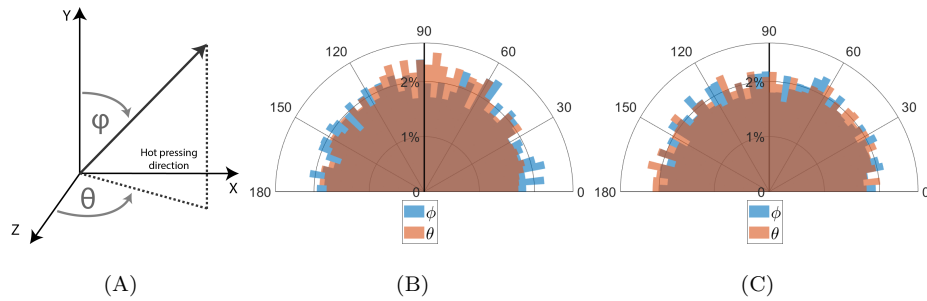


Figure 5: A) Spherical coordinate convention for orientation. B) AD85 nearest neighbor orientation polar histogram. C) AD85 pore major axis orientation polar histogram. The blue and orange represent the ϕ and θ distributions, respectively. The black line at 90° represents the long dimension of the sample.

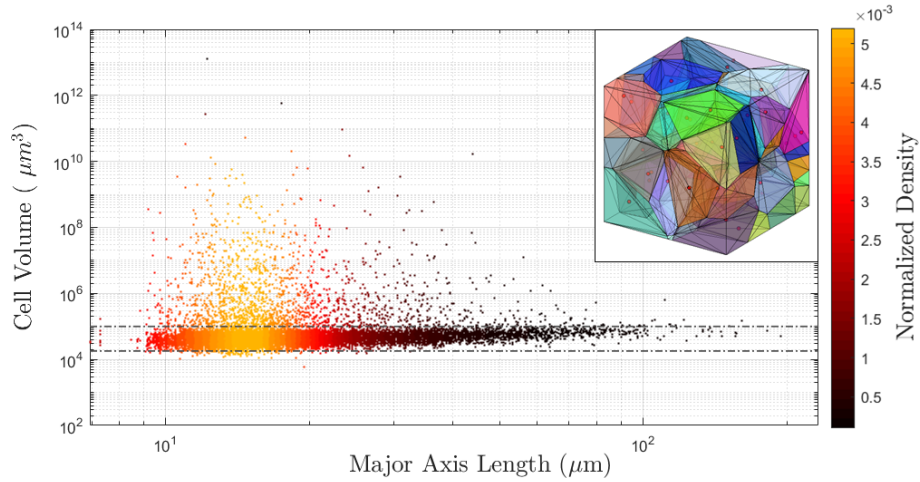


Figure 6: Log-log plot of Voronoi cell volume as a function of pore major axis length in AD85. Contour shows normalized density. Dashed lines indicate boundaries to the high frequency band where the majority of data points lie. The inset is a visualization of Voronoi tessellation where the red dots are seed points.

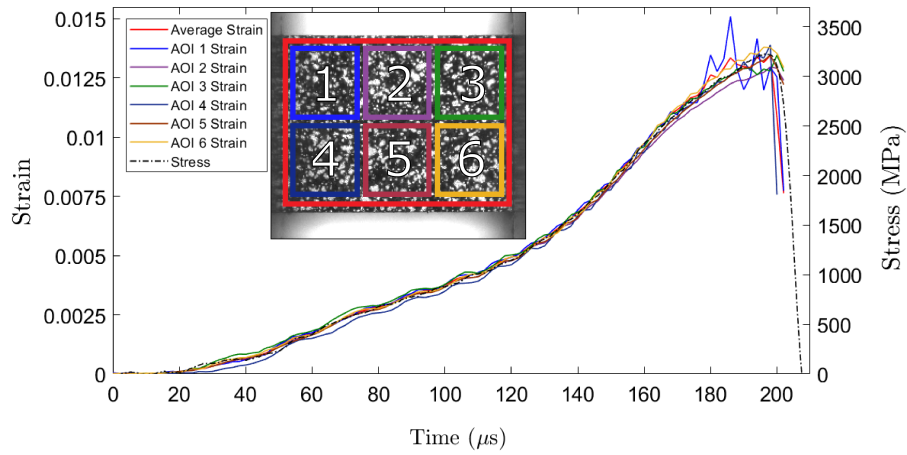


Figure 7: Strain profiles from DIC are matched up to the stress profile computed from the transmitted gauge. The inset shows the area of interest (AOI) each strain profile is computed from. The red strain profile is the average of the entire face.

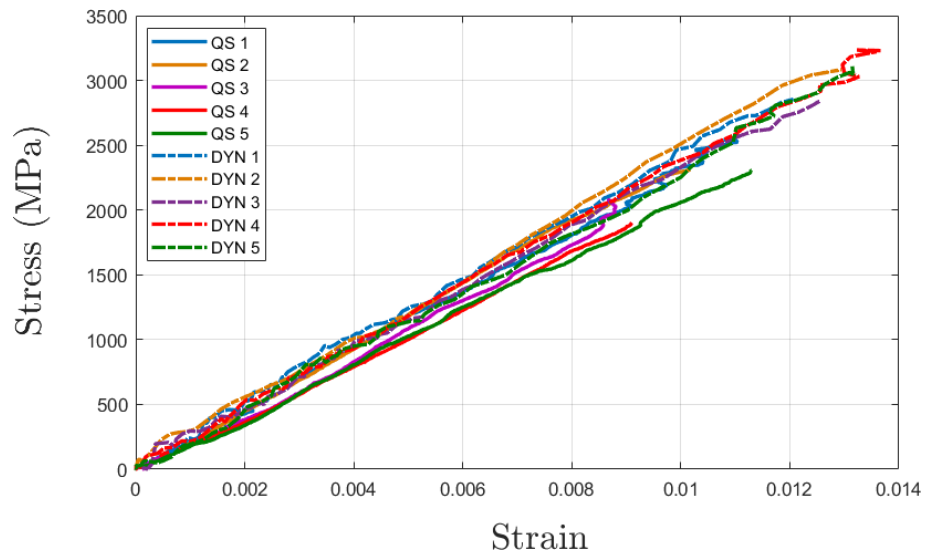


Figure 8: Stress-strain curves for the quasi-static (solid line) and dynamic (dashed line) compression experiments of AD85 alumina.

9. Tables

Table 1: Material properties for AD85 alumina as reported by CoorsTek Inc.[22]

Material	ρ (g/cm ³)	σ_c (GPa)	E (GPa)	ν
AD85 (Al_2O_3)	3.42	1.93	221	0.22

Table 2: Summary of stiffness, strength, and failure strain in quasi-static (QS) and dynamic (DYN) compression experiments with coefficient of variation (COV).

Sample	Stiffness (GPa)	Strength (GPa)	Failure Strain
QS 1	230	2.583	1.10%
QS 2	241	2.311	1.02%
QS 3	227	2.087	0.87%
QS 4	212	1.901	0.91%
QS 5	209	2.306	1.13%
QS Average	224	2.238	1.01%
QS Standard Deviation	12	0.230	0.10%
QS COV	5.30%	10.28%	10.23%
DYN 1	239	2.855	1.21%
DYN 2	241	3.146	1.29%
DYN 3	234	2.844	1.26%
DYN 4	237	3.230	1.37%
DYN 5	224	3.109	1.31%
DYN Average	235	3.037	1.29%
DYN Standard Deviation	6	0.158	0.05%
DYN COV	2.54%	5.20%	4.17%